ACCSCIENCE PUBLISHING

Materials Science in Additive Manufacturing

ORIGINAL RESEARCH ARTICLE

Influence of gas metal arc welding-based wire arc additive manufacturing deposition modes on the hardness, wear, and corrosion behavior of Al5356 walls

Eneko Villabona[1], Fernando Veiga[1*], Alfredo Suárez[2], Eider Aldalur[2], and Pedro Rivero[1,3]

[1]Department of Engineering, ETSIIIT, Public University of Navarra, Campus Arrosadía, Pamplona, Navarra, Spain

[2]Advanced Manufacturing Department, TECNALIA, Basque Research and Technology Alliance, San Sebastián, Spain

[3]Institute for Advanced Materials and Mathematics (INAMAT2), Public University of Navarra, Campus Arrosadía, Pamplona, Navarra, Spain

***Corresponding author:** Fernando Veiga (fernando.veiga@unavarra.es)

Citation: Villabona E, Veiga F, Suarez A, Aldalur E, Rivero P. Influence of gas metal arc welding-based wire arc additive manufacturing deposition modes on the hardness, wear, and corrosion behavior of Al5356 walls. *Mater Sci Add Manuf.* 2026;5(3):026110018. doi: 10.36922/MSAM026110018

Received: March 11, 2026

Revised: April 16, 2026

Accepted: April 21, 2026

Published online: May 21, 2026

Abstract

Wire arc additive manufacturing (WAAM) is a promising technique for producing large-scale aluminum components, although the deposition mode strongly affects thermal history, microstructure, and defect formation. This work investigates the influence of three gas metal arc welding (GMAW)-based WAAM modes (pulsed GMAW, cold arc, and pulsed alternating current [AC]) on the microstructure, hardness, wear, and corrosion behavior of Al5356 walls. Differences in heat input and arc characteristics led to variations in grain size and porosity. Pulsed AC showed the largest grain size and the lowest porosity; pulsed GMAW showed intermediate grain size and the highest porosity; and cold arc exhibited the finest microstructure with intermediate porosity. Magnesium segregation at grain boundaries was observed in all conditions, with possible formation of β (Al_3Mg_2) phase under localized thermal exposure. Hardness values were similar for all samples, although pulsed AC exhibited slightly lower and more homogeneous hardness due to its coarser microstructure. Tribological behavior showed no clear differences among deposition modes. Electrochemical testing revealed that pulsed AC provided the best corrosion resistance, attributed to its reduced porosity and lower grain boundary density, which limits intergranular attack. Overall, deposition mode primarily influences microstructure and corrosion behavior, while its effect on wear performance is limited under the studied conditions.

Keywords: Wire arc additive manufacturing; Al5356; Microstructure; Porosity; Intergranular corrosion; Heat input; Wear behavior

1. Introduction

Wire arc additive manufacturing (WAAM) is classified as a directed energy deposition technology within the family of metal additive manufacturing processes.[1] This technique is conceptually similar to automated arc welding, as it relies on an electric arc to melt a metallic wire feedstock that is deposited layer by layer to build near-net-shape metallic components. Depending on the welding power source and arc characteristics, WAAM processes are commonly categorized as gas metal arc welding (GMAW),[2] gas tungsten arc welding,[3] or plasma arc welding.[4,5] Among these variants, GMAW-based WAAM is particularly attractive due to its high deposition rates and industrial applicability.[6] In this configuration, the wire acts as a consumable electrode and is fed coaxially with the welding torch during deposition.

Aluminum alloys represent a highly attractive material choice for the fabrication of large-scale components by WAAM, owing to their low density, high specific strength, and good corrosion resistance.[7,8] These attributes have led to the increasing adoption of aluminum WAAM components in sectors such as aerospace, shipbuilding, and automotive manufacturing.[9,10] In the present work, aluminum alloy 5356 (Al5356) is selected as the feedstock material. As a member of the 5xxx series, Al5356 is primarily alloyed with magnesium and is well known for its excellent weldability and corrosion resistance, making it particularly suitable for processing via WAAM.[11,12]

This study builds on previous work,[13,14] in which Al5356 walls were fabricated using three different GMAW-based WAAM operating modes recommended by equipment manufacturers: pulsed GMAW, cold arc, and pulsed alternating current (pulsed AC). These modes differ mainly in their current waveforms, which lead to differences in heat input and metal transfer mechanisms. Pulsed GMAW employs a modulated current that enables metal transfer in the form of small droplets, providing improved control over heat input and arc stability. The cold arc mode, in contrast, is characterized by a short-circuit–controlled metal transfer mechanism, which results in a reduced heat input. Both pulsed GMAW and cold arc operate with positive current polarity, whereas the pulsed AC mode alternates the current polarity, allowing control over both arc stability and thermal distribution during the deposition process.

Aldalur *et al.*[13] demonstrated that the selected operating modes lead to noticeable differences in the microstructural features and porosity levels of the deposited material. In particular, the pulsed AC mode resulted in the largest average grain size. Regarding porosity, the pulsed GMAW condition exhibited the highest porosity levels, while the pulsed AC mode showed the lowest. Nevertheless, for all three transfer modes, the observed pores were relatively small, with the volume of most pores being below 5.7×10^{-3} mm^3. This observation suggests that the porosity is mainly associated with cavities formed by hydrogen gas trapped during the solidification process.[14]

Given these marked differences in microstructure and porosity, the objective of the present study is to investigate whether such variations translate into measurable changes in key functional properties of WAAM-fabricated Al5356 components. In particular, this work focuses on assessing the influence of the deposition mode on hardness, wear resistance, and corrosion behavior, thereby providing a more comprehensive evaluation of the performance of Al5356 WAAM walls produced under different GMAW-based operating conditions.

2. Materials and methods

2.1. Material and manufacturing

The walls were manufactured using a 3+2-axis WAAM system manufactured by Addilan (Addilan V0.1, Spain) and equipped with an EWM AC Titan XQ 400 welding power source (EWM, Germany). Three different operating modes of the welding source were comparatively investigated: pulsed GMAW, cold arc, and pulsed AC.

The feedstock material consisted of commercial Al5356 wire with a diameter of 1.2 mm, whose chemical composition is reported in Table 1. The substrate material was also Al5356, supplied in the form of plates with a thickness of 15 mm. The deposited walls were produced as single-bead walls, with dimensions of 100 mm in length and 50 mm in height. Prior to deposition, the aluminum substrates were mechanically polished and cleaned to remove surface oxides and contaminants. During fabrication, pure argon (100 % Ar) was used as the shielding gas at a flow rate of 30 L/min.

Deposition was performed using a bidirectional strategy. Each layer was deposited in a single pass, and the subsequent layer was deposited in the opposite direction once the starting point, corresponding to the end point of the previous bead, reached a temperature of 250 °C, as monitored by a pyrometer. The main processing parameters used for wall fabrication are summarized in Table 2. For all conditions, the wire feed rate was fixed at 8 m/min and the travel speed at 65 cm/min, resulting in a material deposition rate of 1.44 kg/h. The specific voltage and current values corresponding to each operating mode are also reported in Table 2.

As described in Aldalur *et al.*,[13] a high-frequency acquisition system was used to record instantaneous current and voltage signals during deposition. These signals were processed to obtain representative average values of current and voltage for each deposition mode, which are reported in Table 2. In addition, the linear heat input (*HI*)

Table 1. Chemical composition of the Al5356 welding wire

Element	Si	Fe	Cu	Mn	Mg	Cr	Zn	Ti	Be	Al
wt.%	0.05	0.11	0.001	0.16	4.8	0.12	0.001	0.081	0.0001	Bal.

Table 2. Processing parameters used for wall fabrication

Parameter	Pulsed GMAW	Cold arc	Pulsed AC
WFR (m/min)	8	8	8
TS (cm/min)	65	65	65
DR (kg/h)	1.44	1.44	1.44
I (A)	136.75	136.84	128.36
V (V)	17.99	15.35	16.61
HI (kJ/cm)	2.04	1.75	1.89

for each deposition mode was calculated using Equation 1, based on the average power from the instantaneous electrical signals:

$$HI = \frac{\eta \cdot \sum_{i=1}^{n} \frac{Ii \cdot Vi}{n}}{TS} \quad (1)$$

where Ii (A) and Vi (V) are the instantaneous current and voltage values, respectively; TS is the travel speed (cm/s); and η is the arc thermal efficiency. A constant efficiency value of 0.9 was assumed, in agreement with values reported in previous studies.[13,15] The resulting heat input values are also included in **Table 2** for comparison.

2.2. Microstructural analysis

Specimens for microstructural examination were machined from each fabricated wall. Analysis was performed on the plane defined by the building and deposition directions, corresponding to the orientation used for subsequent testing. Samples were mounted, mechanically ground, and polished following standard metallographic procedures, and etched for 30 seconds using Keller's reagent (95 mL H_2O, 2.5 mL HNO_3, 1.5 mL HCl, 1 mL HF; ES Laboratory, USA). Microstructural characterization was conducted using optical microscopy (BX60M, Olympus, Japan) and scanning electron microscopy (SEM) with energy-dispersive X-ray spectroscopy (EDX) on a Zeiss system (EVO 15, Zeiss, Germany).

2.3. Corrosion test

To evaluate the corrosion resistance of the aluminum walls, potentiodynamic polarization (PDP) tests were performed. As illustrated in Figure 1B, the electrochemical measurements were carried out using a Gamry potentiostat (Gamry Reference 600, Gamry Instruments, USA) in a conventional three-electrode configuration, comprising an Ag/AgCl (3 M KCl) reference electrode, a platinum counter electrode, and the specimen acting as the working electrode. All experiments were conducted at room temperature in a 0.6 M NaCl aqueous solution. The exposed area of the working electrode was fixed at 0.49 cm^2, and for each condition, measurements were repeated three times to ensure reproducibility and statistical reliability.

Prior to testing, the samples were sequentially ground using SiC abrasive papers from 120 to 2,000 grit (Struers, Denmark), followed by mirror polishing with a 3 μm diamond suspension. Before initiating the polarization scan, the open circuit potential was allowed to stabilize for 900 s. Subsequently, the PDP scans were performed starting at −300 mV relative to the stabilized open circuit potential and continued anodically until either a potential of 1 V or a current density of 0.25 A/cm^2 was reached. The potential was swept at a constant scan rate of 0.16 mV/s. From the obtained polarization curves, the electrochemical parameters were determined using the Tafel extrapolation method by fitting the linear regions of both anodic and cathodic branches in the semi-logarithmic representation. The extrapolation was performed over at least one decade of current density within the Tafel-linear region, avoiding diffusion-controlled and transition regions.

2.4. Hardness measurement

The hardness of the samples was measured using a Mitutoyo MicroWizHard microhardness tester (Mitutoyo HM-210/220 Type A, Japan). Measurements were performed at three different locations along each wall: the left side (wall start), the central region, and the right side (wall end). At each location, 10 indentations were carried out under a load of 0.5 kgf.

2.5. Tribology test

The tribological behavior of the WAAM-fabricated Al5356 specimens was evaluated under dry sliding conditions using pin-on-disk tests with a Microtest MT Series tribometer (MT Series Pin-on-Disk Tribometer, Microtest, Spain), following the guidelines of the ASTM G99-17 standard.[16] As shown in Figure 1C, a spherical counterbody with a diameter of 6 mm made of high-carbon chromium steel (100Cr6, AISI 52100) was employed. All tests were conducted under a constant normal load of 10 N, a rotational speed of 200 rpm, and a wear track radius of 8 mm, resulting in a total sliding distance of 100 m. Prior to testing, the specimens were mechanically polished to achieve a uniform surface roughness of Ra = 3 µm to minimize the influence of initial surface topography. The coefficient of friction (COF) was continuously recorded and calculated as the instantaneous ratio between the tangential and normal forces, in accordance with ASTM G99-17.[16] Material loss was quantified by volumetric evaluation. The wear track volume was determined by measuring three different segments of the wear scar using confocal microscopy (S mart, Sensofar, Spain). These measurements were then extrapolated to estimate the total wear track volume, and the average value was calculated. Once the wear volume generated during the

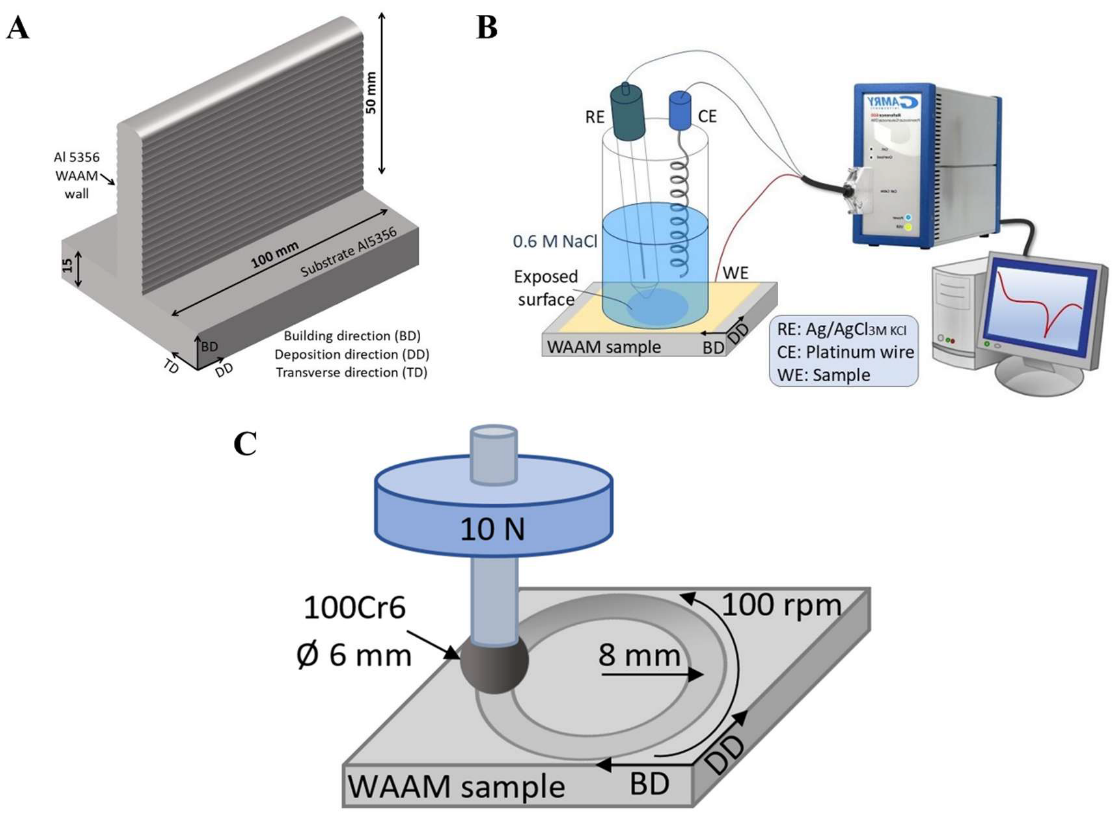

Figure 1. Schematic representation of (A) the manufactured wall; (B) the experimental setup for the potentiodynamic polarization tests and (C) a pin-on disk test

Abbreviations: CE: Counter electrode; RE: Reference electrode; WAAM: Wire arc additive manufacturing; WE: Working electrode.

test was determined, the wear coefficient of the material (k, in $mm^3/N \cdot m$) was calculated according to **Equation 2**, defined as the ratio between the wear volume (V, in mm^3) and the product of the applied normal load (F, in N) and the sliding distance (s, in m).

$$k = \frac{V}{F \cdot s} \tag{2}$$

3. Results

3.1. Microstructure

According to the Al–Mg phase diagram and considering the chemical composition of the Al5356 wire, which contains less than 5 wt.% Mg, the formation of β-Al_3Mg_2 intermetallic compounds is expected.[17] The metallographic analysis revealed that, regardless of the deposition mode employed, the microstructure of the WAAM-fabricated Al5356 walls consists of an α-Al matrix with noticeable Mg segregation at grain boundaries and interdendritic regions. Such compositional heterogeneity may lead to the formation of β (Al_3Mg_2) phase precipitates, particularly under the thermal cycling conditions inherent to the WAAM process.[18]

Figure 2, corresponding to the sample fabricated using the pulsed GMAW mode, shows a high-magnification image of the grain boundary region. These areas appear more strongly attacked by Keller's reagent, which highlights the presence of compositional heterogeneities at the grain boundaries. The EDX analysis performed in the region shown in Figure 2C confirms a higher Mg concentration at the grain boundaries compared with the surrounding α-Al matrix. This behavior is attributed to Mg segregation during solidification and thermal cycling inherent to the WAAM process, which may lead to the formation of β (Al_3Mg_2) phase precipitates in interdendritic and grain boundary regions under suitable local conditions.

Figure 3 shows the microstructures of the three fabricated walls. As previously observed in the electron backscatter diffraction analysis reported in our earlier work,[13] the pulsed AC sample exhibited the largest average grain area, approximately 2,300 μm^2, whereas the cold arc condition presented the finest microstructure, with an average grain area of 1,046 μm^2. The pulsed GMAW condition showed an intermediate grain area, around 1,900 μm^2. Nevertheless, as can be observed in Figure 3D, the central region of each deposited layer exhibits a larger grain area and a lower amount of Mg-rich regions and/or possible β-phase compared with the remelting zones between adjacent layers. Furthermore, the remelting zones highlighted in Figure 3D show a more pronounced response to the etchant and a higher pore density than the central regions of the deposited layers, indicating greater microstructural heterogeneity in these areas. This difference is associated with the repeated thermal cycles inherent to the WAAM process, which promote solute redistribution and phase precipitation in the reheated areas. Previous studies[17] have also reported that the Mg content in WAAM-fabricated Al5356 walls is lower than that in the original feedstock wire, due to Mg evaporation during deposition. In localized regions, the process temperature may exceed the boiling point of Mg (above 1,100 °C), leading to partial Mg loss and compositional changes in the deposited material.

In addition to the Al–Mg phases, trace alloying elements such as Fe present in the welding wire may lead to the formation of Fe-rich intermetallic compounds. Figure 4 shows an EDX line scan performed across a brighter region identified in the high-definition backscattered electron (HD-BSD) detector image. The corresponding compositional profile reveals a local decrease in the Al and Mg signals and a simultaneous increase in the Fe signal relative to the surrounding matrix. These observations suggest the presence of Fe-containing intermetallic particles, which may correspond to phases such as $Al_6(Fe,Mn)$, Al_3Fe, or $Al_2(Fe,Mn)$.[19,20] Such particles may locally influence the mechanical and corrosion behavior of the material by acting as preferential sites for stress concentration or microgalvanic coupling.

Figure 5 shows the pore distribution observed in the samples used for the corrosion tests prior to exposure. Clear differences in porosity levels can be identified among the three deposition modes. The pulsed GMAW condition exhibits the highest porosity level, reaching 2.75%, with the presence of several relatively large pores with diameters of approximately 150 μm. However, the porosity distribution within the wall is not completely homogeneous, and some regions of the same sample show markedly lower porosity levels, close to 1%. The cold arc condition presents a lower overall porosity level (1.71%), characterized by fewer large pores but a higher density of micropores distributed throughout the microstructure. In contrast, the pulsed AC condition shows the lowest porosity level (0.66%), with both a reduced number of pores and smaller pore sizes.

In WAAM Al5356, microstructural evolution and defect formation are strongly influenced by the interplay between process thermal conditions and the inherent characteristics of the arc associated with each deposition mode. Although the calculated heat input values (2.04, 1.89, and 1.75 kJ/cm for pulsed GMAW, pulsed AC, and cold arc, respectively) indicate moderate differences, they provide a useful framework to interpret the resulting

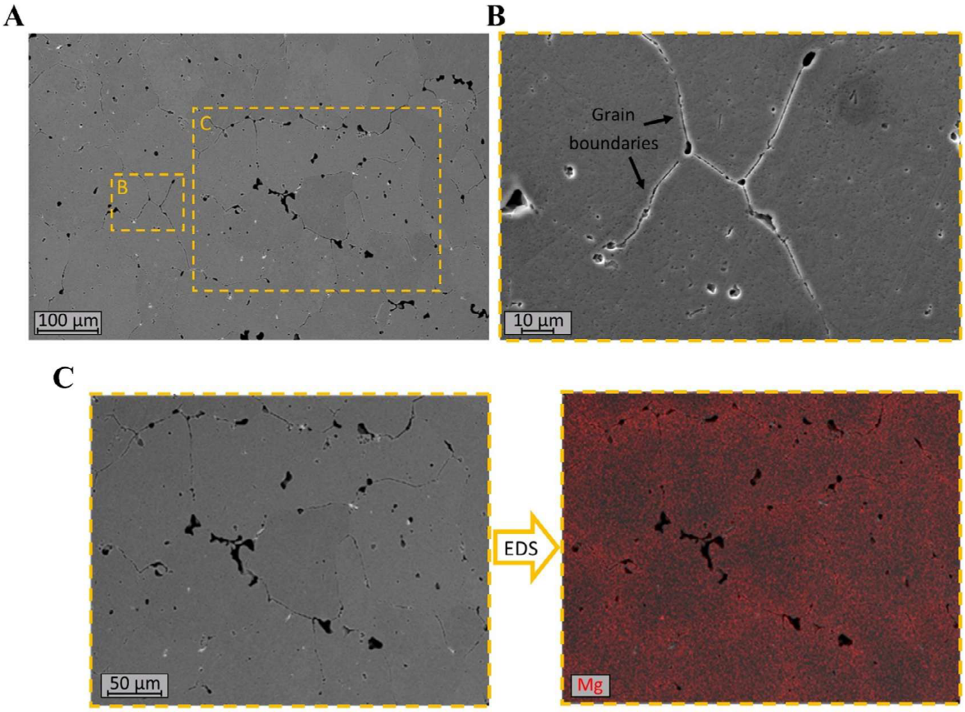

Figure 2. Scanning electron microscopy characterization of the pulsed GMAW condition: (A) Representative microstructure (scale bars: 100 µm; magnification: 400×), (B) high-magnification image of a grain boundary region (scale bars: 10 µm; magnification: 2,000×), and (C) Energy-dispersive X-ray spectroscopy analysis of a selected region from (A) (scale bars: 50 µm; magnification: 750×)

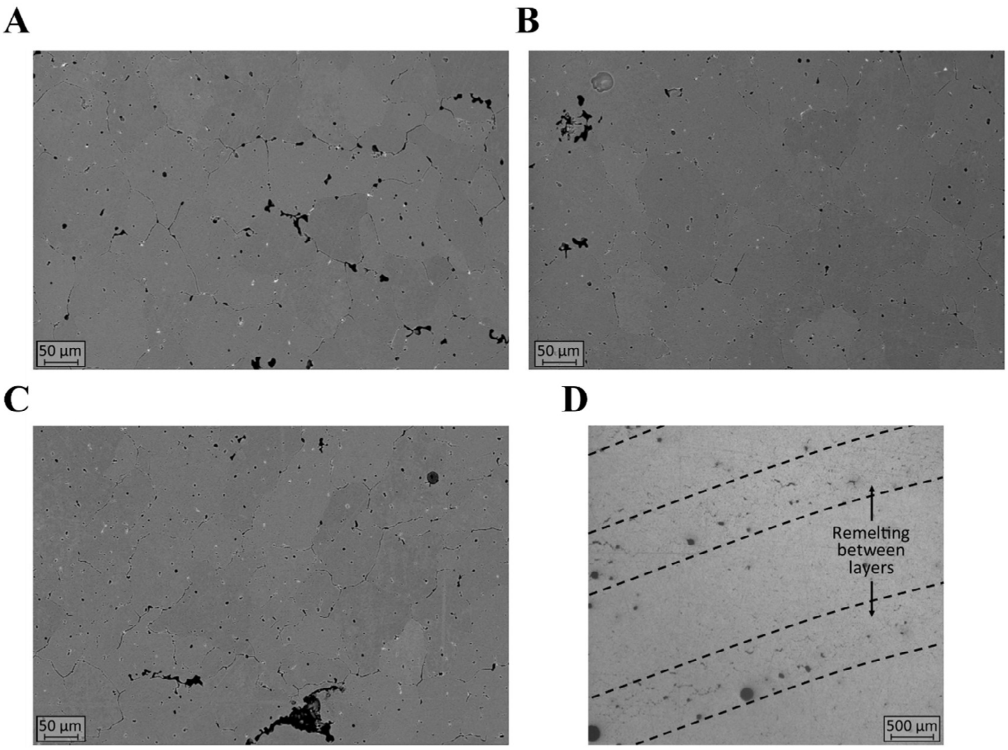

Figure 3. Representative scanning electron micrographs showing the microstructures of the walls fabricated under (A) pulsed GMAW, (B) cold arc, and (C) pulsed AC modes, together with (D) an optical micrograph highlighting the melt zones. Scale bars: 50 µm/500 µm; magnification: 400×/1.25×.

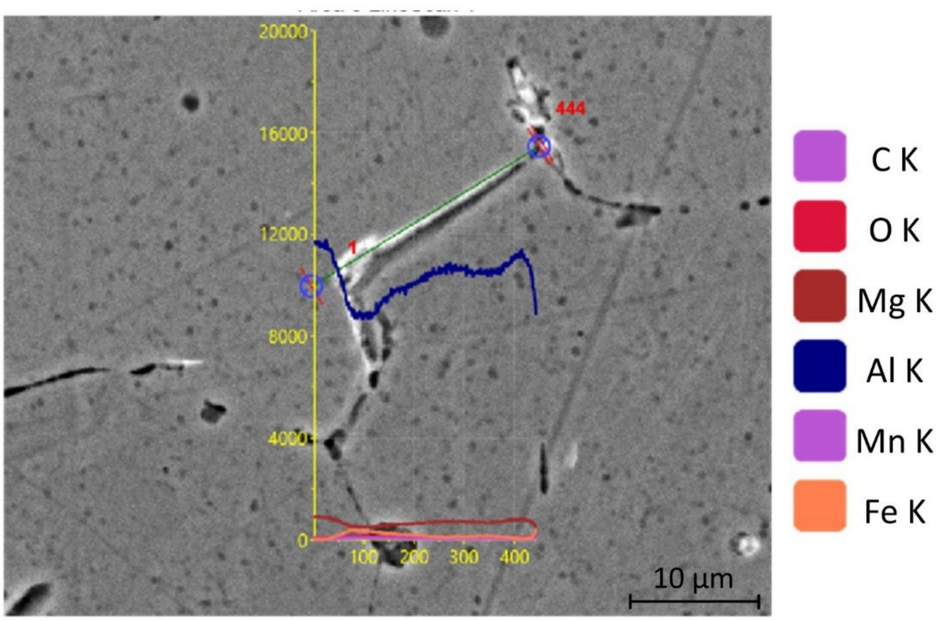

Figure 4. Energy-dispersive X-ray spectroscopy line scan across a bright intergranular precipitate region

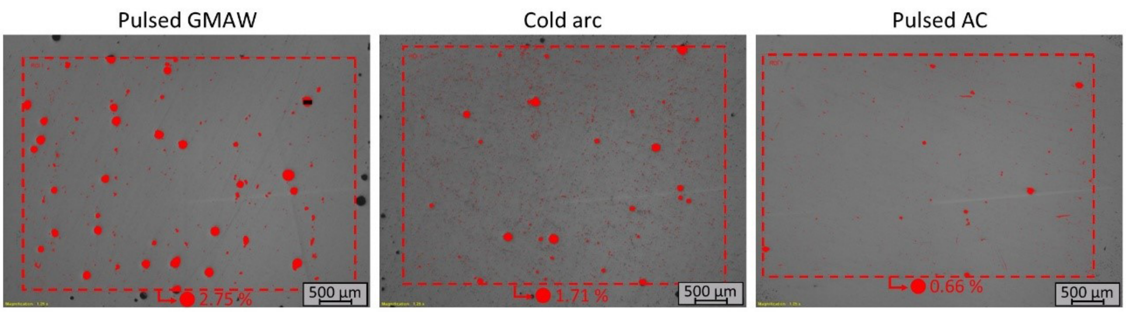

Figure 5. Porosity quantification by image analysis of optical micrographs of the wire arc additive manufacturing-fabricated samples. Scale bars: 500 µm; magnification: 1.25×.

thermal histories. The higher heat input in the pulsed GMAW condition promotes slower cooling rates, which favor grain growth and enhance solute redistribution. In contrast, the lower heat input of the cold arc mode leads to faster solidification and a more refined microstructure, while the pulsed AC condition exhibits an intermediate thermal behavior.

However, beyond these thermal effects, the intrinsic characteristics of each arc mode play a decisive role. The finer grain structure observed in the cold arc condition can be associated with its controlled short-circuit transfer mode, which results in a less energetic and more stable metal transfer, limiting melt pool agitation and promoting rapid solidification. Conversely, the larger grain size measured in the pulsed AC condition is not only consistent with its intermediate heat input but also with the effect of alternating polarity. During the negative current phase, electron flow towards the electrode induces additional heating of the previously deposited material, effectively increasing the local thermal exposure and promoting grain coarsening. This reheating effect is absent in the pulsed GMAW mode, where the current remains strictly positive.

Regarding defect formation, particularly porosity, both heat input and metal transfer dynamics must be considered. While lower heat input generally limits the time available for gas escape, the layer-by-layer thermal accumulation inherent to WAAM can partially compensate for this effect, especially in the cold arc condition. In this case, the combination of reheating between layers and a controlled, less aggressive droplet transfer mechanism favors a more stable melt pool, facilitating gas escape and resulting in relatively low porosity levels. In contrast, the spray-like transfer characteristic of pulsed GMAW and pulsed AC modes, driven predominantly by electromagnetic forces, generates a more turbulent melt pool, which can promote gas entrapment. Nevertheless, the pulsed AC mode benefits from polarity reversal, which disrupts the oxide layer and enhances hydrogen degassing, contributing to its comparatively lower porosity.

Overall, these results indicate that the microstructural evolution and defect formation in WAAM Al5356 are governed by a complex interplay between heat input, thermal cycling, and arc physics.

3.2. Corrosion

The differences in porosity, microstructure, and Mg segregation identified in the previous section are expected to affect the corrosion behavior of the material, as both pre-existing pores and Mg-enriched grain boundary regions may act as preferential sites for electrolyte accumulation and localized corrosion initiation. To evaluate the corrosion resistance of the aluminum walls, PDP tests were performed.

Figure 6 presents the PDP curves obtained from the electrochemical tests conducted in 0.6 M NaCl solution. In the cathodic region, all samples exhibit similar slopes, indicating comparable cathodic kinetics and confirming that the electrochemical response is predominantly controlled by charge-transfer processes rather than by diffusion limitations. Upon anodic polarization, the current density initially remains low, which is associated with the formation of a surface oxide film. However, this regime is narrow and unstable, as evidenced by the continuous increase in current density with increasing potential. The absence of a well-defined passive range indicates limited passivation; consequently, shortly after exceeding the corrosion potential, a sharp rise in current density is observed, signaling the onset of active corrosion.

Within each material condition, the three polarization curves show good reproducibility, indicating a consistent electrochemical response. An exception is observed for the cold arc condition, where the third curve is shifted toward higher current densities, approximately one order of magnitude greater than the other two measurements. This shift reflects increased corrosion activity for that specific test and explains the higher standard deviation observed in the corrosion current density for this condition.

The electrochemical parameters obtained from the polarization tests are summarized in Table 3 in terms of mean values and standard deviations of the corrosion potential (E_{corr}) and corrosion current density (I_{corr}). The three aluminum conditions exhibit comparable corrosion potentials, with mean E_{corr} values ranging from −0.76 to −0.73 V, indicating similar thermodynamic tendencies toward corrosion. Pulsed GMAW shows the most negative average E_{corr} (−0.759 V), whereas cold arc and pulsed AC present slightly nobler values, although the differences remain within a relatively narrow potential window.

More pronounced differences were observed in I_{corr}. Cold arc showed the highest mean I_{corr} (2.92×10^{-6} A/cm^2), suggesting the lowest corrosion resistance among the three conditions, while pulsed AC showed the lowest I_{corr} (8.36×10^{-7} A/cm^2), indicative of improved corrosion performance. Pulsed GMAW presented an intermediate behavior with an average I_{corr} of 1.54×10^{-6} A/cm^2. Pulsed AC also displayed the lowest dispersion in I_{corr}, suggesting a more homogeneous electrochemical response. Nevertheless, all conditions exhibit relatively low corrosion current density values, which indicates that the corrosion rates are expected to be low under the tested conditions. This suggests that, despite the limited passivation behavior observed in the polarization curves, the overall corrosion kinetics of the WAAM-fabricated aluminum samples in 0.6 M NaCl solution remain moderate to low. Overall, these results indicate that, while the corrosion potentials are broadly similar, the corrosion kinetics are more affected by the specific processing condition, with the pulsed AC sample exhibiting the most favorable corrosion behavior and the lowest mean I_{corr} among the three conditions. Ultimately, pores act as surface irregularities that serve as preferential sites for corrosive attack;[21-24] therefore, an increased pore density leads to a reduction in the corrosion resistance of the material. Consequently, the lower porosity observed in the pulsed AC wall,[13] attributed to the variable polarity characteristic of this process, results in improved corrosion performance in aggressive environments.

Table 3. Electrochemical parameters extracted from potentiodynamic polarization curves

Condition	E_{corr} (V)	I_{corr} (A/cm^2)
Pulsed GMAW	−0.759 ± 0.014	$1.54 \times 10^{-6} \pm 7.86 \times 10^{-7}$
Cold arc	−0.725 ± 0.010	$2.92 \times 10^{-6} \pm 3.52 \times 10^{-6}$
Pulsed AC	−0.726 ± 0.030	$8.36 \times 10^{-7} \pm 3.00 \times 10^{-7}$

There are limited published studies specifically addressing the corrosion resistance of Al5356 alloys fabricated by WAAM. Nevertheless, when comparing

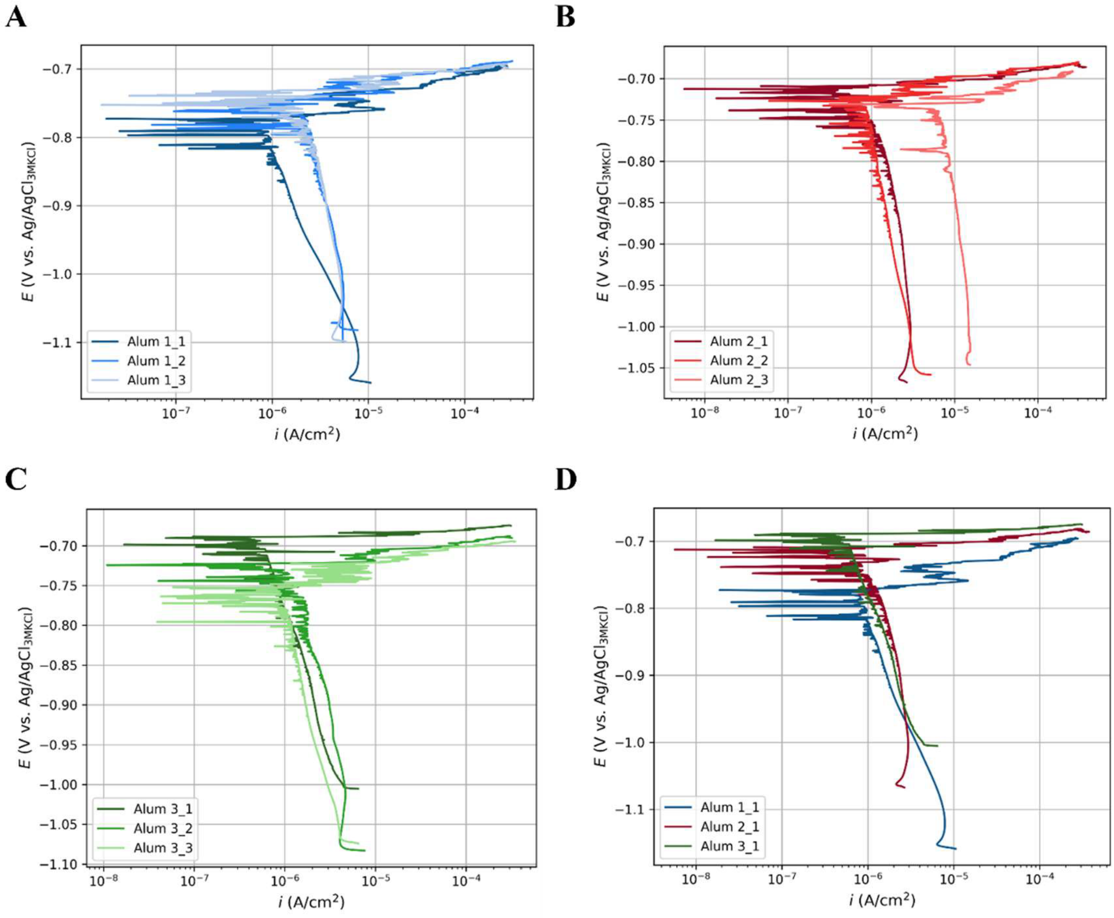

Figure 6. Potentiodynamic polarization curves of Al5356 wire arc additive manufacturing walls fabricated by (A) pulsed GMAW, (B) cold arc, and (C) pulsed AC conditions in 0.6 M NaCl solution. (D) Comparison of the three deposition modes.

the present results with available literature, Liang *et al.*[18] reported corrosion current densities in the range of 2–9 $\times 10^{-6}$ A/cm^2 for WAAM-fabricated Al5356. Furthermore, comparable corrosion current densities have been reported for other aluminum alloys produced by WAAM; for instance, Wang *et al.*[25] observed corrosion current values of the same order of magnitude (6.61×10^{-6} A/cm^2) for WAAM-fabricated Al2319.

Figure 7 shows representative corrosion morphologies of the samples after corrosion testing, where evidence of intergranular corrosion can be observed. The attack is preferentially concentrated along the grain boundaries, indicating that these regions are more susceptible to corrosion than the surrounding α-Al matrix. This behavior is associated with Mg segregation at grain boundaries and the possible formation of the β (Al_3Mg_2) phase under localized sensitization conditions induced by thermal cycling inherent to the WAAM process, as previously identified by the metallographic and EDX analyses. Due to the compositional contrast between Mg-enriched boundary regions (and possible β-Al_3Mg_2 precipitation) and the surrounding α-Al matrix, local galvanic coupling can be established, promoting preferential dissolution along grain boundaries. As a result, the corrosion process propagates following the grain boundary network, leading to the characteristic intergranular attack observed in the micrographs. This mechanism is consistent with the known corrosion behavior of Al–Mg alloys, in which Mg-rich intermetallic phases can reduce the local stability of the passive oxide film and facilitate localized degradation.

Figure 7 also reveals cases in which pre-existing WAAM pores appear to act as preferential corrosion initiation sites. In the image, a large central cavity, likely corresponding to an original solidification pore, is surrounded by irregular attack features extending outward from the pore edges. This morphology suggests that corrosion initiated at the pore surface and subsequently propagated along grain boundaries or interdendritic regions. Such behavior is consistent with the segregation of Mg and the presence of β (Al_3Mg_2) phase at grain boundaries, which promotes localized galvanic effects and facilitates intergranular corrosion propagation.

The localized intergranular corrosion mechanisms identified at the microscale by SEM are further corroborated at a larger scale by optical microscopy, which highlights differences in corrosion severity among the various deposition conditions. Comparisons of the surface morphologies after corrosion testing for the three types of samples are shown in Figure 8. In all cases, the exposed regions, delimited by dashed lines, exhibit both pre-existing pores and a distribution of small corrosion pits across the surface. These pits are interpreted as the surface manifestation of localized attack at Mg-enriched grain boundary regions and/or selectively dissolved β-Al_3Mg_2 particles, in agreement with intergranular corrosion features observed by SEM. For the cold arc condition, the apparent higher density of small pits can be related to its finer grain structure, which increases the total grain boundary area and, consequently, the number of potential sites for Mg segregation and β-phase precipitation. In addition to this generalized pitting distribution, the cold arc sample also shows localized regions of more severe and irregular attack. At higher magnification, these features appear to result from the coalescence and lateral growth of adjacent pits, suggesting a transition from isolated pit formation to more developed intergranular corrosion pathways. This localized intensification of attack is consistent with the combined effect of high grain boundary density and electrochemical heterogeneity introduced by Mg-rich β-phase distribution.

Prior to the corrosion tests, the pulsed AC sample exhibited a lower porosity level compared with the other

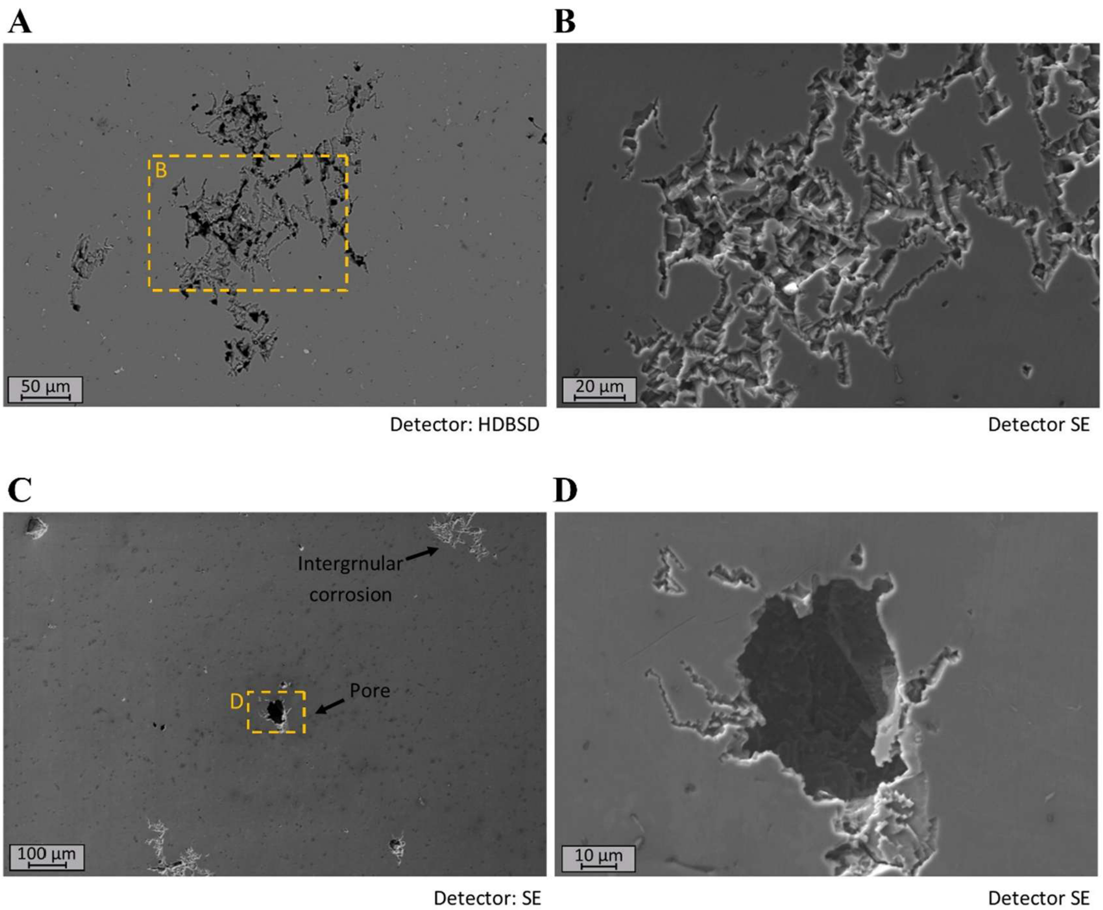

Figure 7. Scanning electron micrographs illustrating corrosion morphology: (A, B) intergranular corrosion features. Scale bars: 50 µm/20 µm; magnification: 500×/1,360×; (C, D) corrosion at a pre-existing pore. Scale bars: 100 µm/10 µm; magnification: 190×/1,700×.

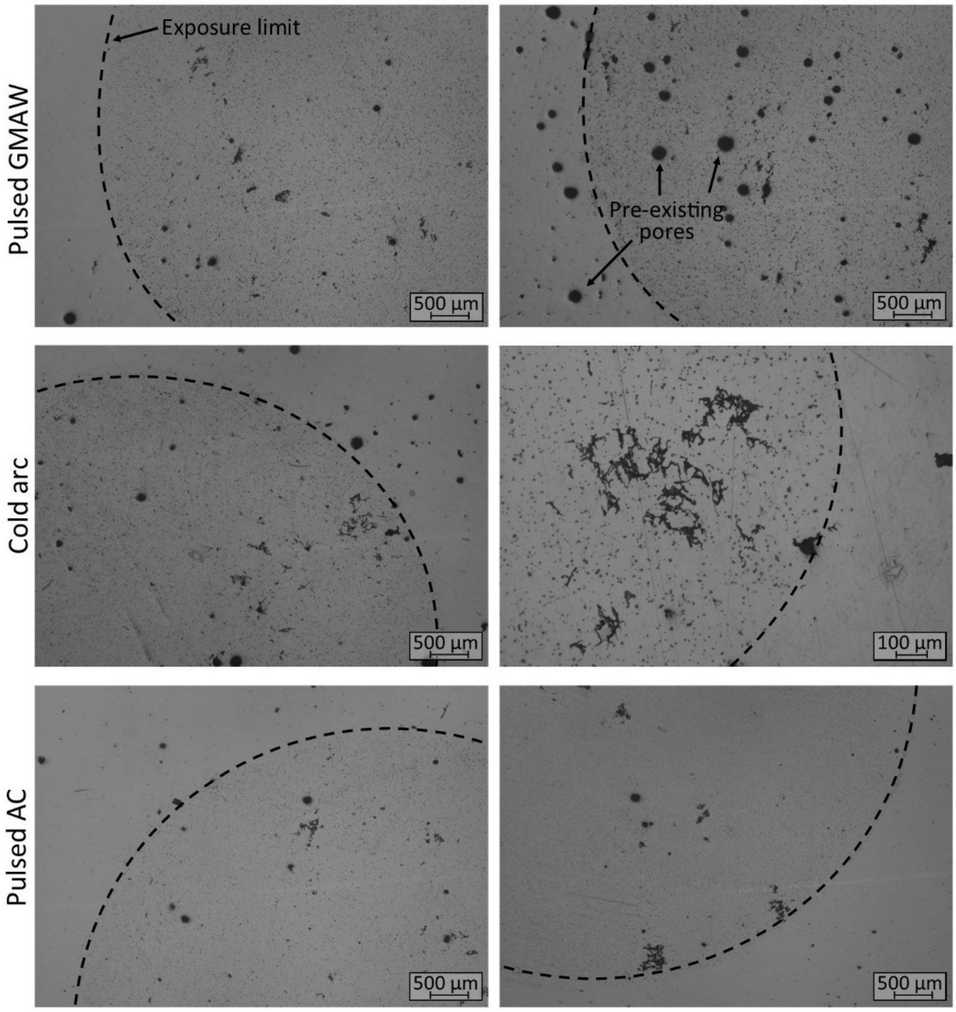

Figure 8. Optical micrographs of the surfaces after corrosion testing for the wire arc additive manufacturing-fabricated Al5356 samples produced using pulsed GMAW, cold arc, and pulsed AC modes. Scale bars: 500 μm/100 μm; magnification: 1.25×/5×.

conditions, which may have reduced the number of potential sites for corrosion initiation and thus contributed to the slightly improved corrosion resistance observed for this deposition mode. In addition, this improved behavior may also be associated with its coarser grain structure, since a larger grain size reduces the overall grain boundary density, thereby limiting the available sites for Mg segregation and possible β-phase precipitation, which in turn decreases the susceptibility to intergranular corrosion.

3.3. Hardness

Figure 9 shows the mean values and standard deviations obtained from the 10 Vickers hardness measurements performed at each analyzed zone of the samples, as well as the overall average hardness calculated from the three zones for each wall. For the pulsed GMAW and cold arc conditions, noticeable differences are observed among the three regions of the wall. In the case of pulsed GMAW, the central region exhibits a markedly higher hardness value (88.88 HV) compared with the lateral zones (76.41 HV and 71.70 HV). Similarly, for the cold arc condition, the left (initial) region of the wall shows a hardness value nearly 20 HV higher than that measured in the other two regions. These variations can be attributed to local microstructural heterogeneities, such as porosity distribution or differences in grain size caused by thermal gradients in the process. Previous studies have shown that pulsed GMAW and cold arc processes tend to generate higher porosity levels, with a non-uniform spatial distribution along the wall.[14] Consequently, local differences in porosity may strongly influence the measured hardness values in different regions.

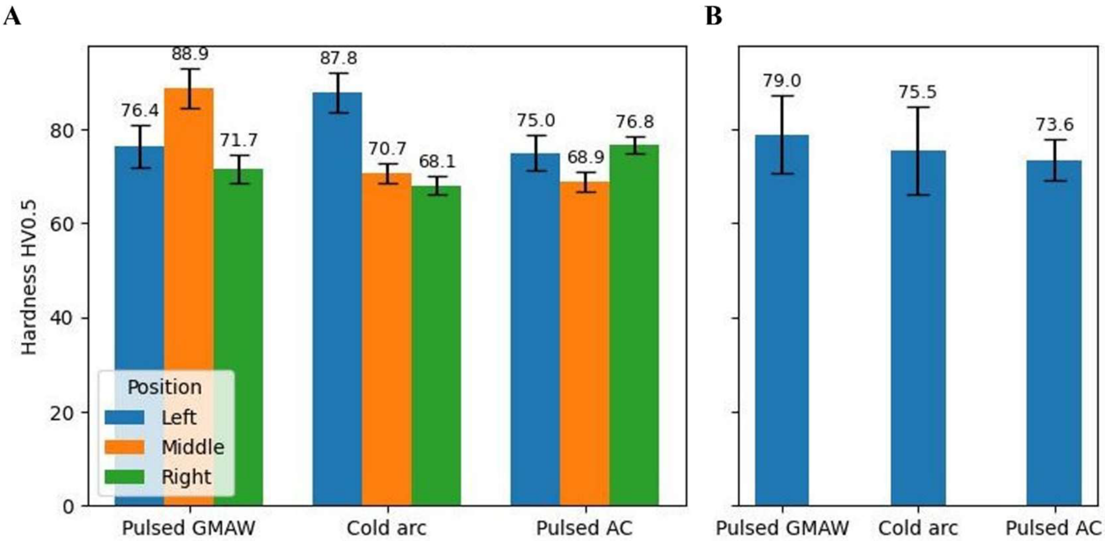

Figure 9. Vickers hardness of the different WAAM-fabricated Al5356 samples: (A) Measured at different wall positions and (B) the corresponding overall average values

When considering the overall hardness, calculated as the average of all three regions of each wall, the pulsed GMAW condition exhibits the highest mean hardness (79 HV), followed by the cold arc condition (75.5 HV), while the pulsed AC condition presents the lowest average hardness (73.6 HV). A review of the literature indicates that the hardness values obtained in the present study are in good agreement with previously reported results for WAAM-fabricated Al5356. Muthukumaran *et al.*[26] reported hardness values close to 80 HV along the deposited wall, whereas Imširović *et al.*[27] reported values around 71 HV. Zuo *et al.*[28] observed hardness values ranging from 69.4 HV to 77.9 HV, depending on the applied heat input. Similarly, Wang *et al.*[29] reported hardness values between 68 and 76 HV, attributing these variations to differences in heat dissipation along the wall, which affect grain size and, consequently, microhardness. Specifically, regions with larger grain sizes and the presence of microporosity were associated with lower hardness values. Sharma *et al.*[30] also concluded that variations in the heat dissipation rate from the bottom to the top regions of the wall lead to changes in microstructure and grain size, resulting in spatial variations in microhardness, with reported values around 70 HV.

The reduced hardness observed for the pulsed AC samples can be attributed to their larger grain size compared with the other conditions, as reported in previous work.[13] In the pulsed AC mode, the alternation of current polarity causes electrons to flow in opposite directions during the negative polarity phase, leading to additional heating of the previously deposited material and promoting grain growth. In addition, the pulsed AC condition shows the lowest hardness dispersion among the three modes. This more homogeneous hardness distribution is likely related to the lower porosity levels achieved with this process, as discussed in the aforementioned studies,[13,14] which contributes to a more uniform microstructure along the wall.

Although the slightly lower hardness measured for the pulsed AC condition can be partly attributed to its larger grain size, in accordance with the Hall–Petch relationship, grain size is not the only factor controlling the hardness of Al5356. In Al–Mg alloys, solid solution strengthening provided by Mg plays a key role in the mechanical response. The metallographic and EDX analyses performed in this study confirmed Mg segregation at the grain boundaries, associated with the precipitation of β (Al_3Mg_2) phase, indicating that local compositional variations also contribute to hardness. In addition, Mg evaporation during WAAM processing has been reported in the literature due to the high temperatures reached in the molten pool, which may locally reduce the solid solution strengthening effect in the α-Al matrix. Since thermal history differs depending on the deposition mode, the extent of Mg redistribution, segregation, and possible evaporation may also vary among conditions. Therefore, the hardness differences observed in this work are likely the result of a combined effect of grain size, local Mg distribution, and porosity, rather than being exclusively governed by grain size alone.

3.4. Tribology

Figure 10 shows the evolution of the COF as a function of sliding distance for the three samples. In all cases, the COF exhibits pronounced fluctuations throughout the test, with values ranging approximately between 0.2 and 1.0. After a short initial running-in stage, the system reaches a quasi-steady-state regime characterized by high instability. This behavior is attributed to adhesive wear mechanisms and to the continuous formation and disruption of a mechanically mixed transfer layer, which is typical of Al–Mg alloys under dry sliding conditions.

As seen in Table 4, among the evaluated conditions, the cold arc sample exhibits the lowest average COF (0.459), whereas the pulsed GMAW condition shows the highest value (0.627). The pulsed AC sample presents an intermediate behavior, with an average COF of 0.582. The standard deviation of the COF is very similar for the three samples, with values close to 0.2, reflecting the strong fluctuations observed during sliding and highlighting the inherently unstable nature of the tribological contact. This suggests that the apparent differences in average COF values are largely masked by the intrinsic fluctuations of the dry sliding contact, and no clear difference among the three conditions can be established.

Table 4. Mean values and standard deviations of the coefficient of friction (COF) obtained under dry sliding conditions

Mode	Pulsed GMAW	Cold arc	Pulsed AC
Value	0.627 ± 0.2	0.459 ± 0.2	0.582 ± 0.2

Table 5 presents the mean values and standard deviations of the wear track volumes measured in the three analyzed regions of each sample, as determined by confocal microscopy and illustrated in Figure 11. Since all tribological tests were performed under identical normal load and sliding distance conditions, the differences in the wear coefficient are directly governed by the volume of material removed from the wear track, as defined in **Equation 2**. Accordingly, the cold arc condition, which exhibits the largest wear track volume, shows the highest wear coefficient, whereas the pulsed AC condition presents

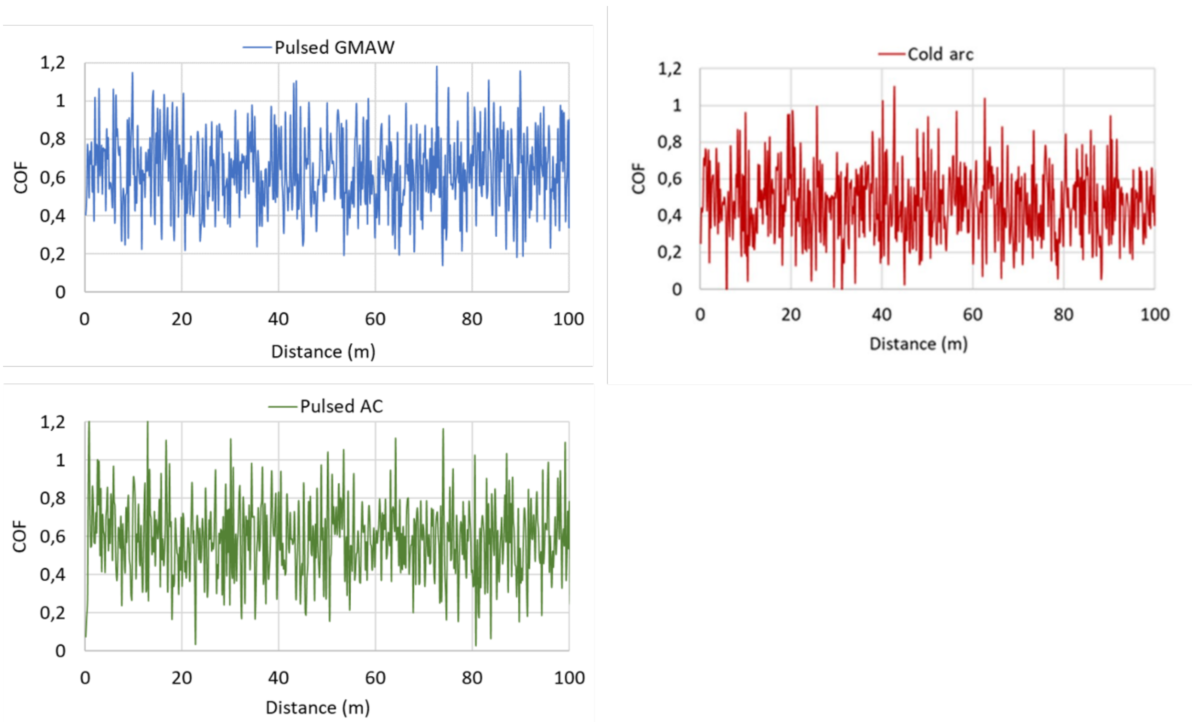

Figure 10. Evolution of the coefficient of friction (COF) as a function of sliding distance for the pulsed GMAW, cold arc, and pulsed AC WAAM-fabricated Al5356 samples under dry sliding conditions

the lowest value. Nevertheless, these differences are relatively small, while the associated standard deviations are comparatively large. As a result, within the experimental scatter, no clear differences in wear resistance can be established among the three deposition modes.

Table 5. Wear track volume measured by confocal microscopy and calculated wear coefficient of the wire arc additive manufacturing-fabricated Al5356 samples under dry sliding conditions

Mode	V_{loss} (mm^3)	Wear coefficient, *k* (mm^3/N·m)
Pulsed GMAW	3.61 ± 0.67	$3.59 \times 10^{-3} \pm 6.7 \times 10^{-4}$
Cold arc	4.33 ± 0.86	$4.30 \times 10^{-3} \pm 8.6 \times 10^{-4}$
Pulsed AC	3.24 ± 0.87	$3.22 \times 10^{-3} \pm 8.7 \times 10^{-4}$

In all cases, the 3D confocal reconstructions shown in Figure 11 reveal well-defined wear scars with clear material removal along the sliding direction. This morphology confirms that wear is dominated by severe plastic deformation and adhesive mechanisms, in agreement with the pronounced fluctuations observed in the COF. The presence of deep grooves and irregular valleys indicates localized material tearing and transfer processes.[31] In addition, material pile-up is observed at the edges of the wear tracks, forming ridges as a consequence of lateral material displacement from within the grooves toward the track boundaries.

Besides the adhesive features, the wear tracks also display longitudinal grooves aligned with the sliding direction, which are characteristic of plowing and abrasive wear mechanisms.[32,33] These grooves are generated by hard asperities or entrapped wear debris acting as third bodies, which penetrate the softer aluminum surface and displace material laterally without immediate removal. The coexistence of these features indicates a mixed wear mechanism, in which adhesive wear is predominant but accompanied by an abrasive contribution.

Figure 12 shows SEM images of a representative wear track after the dry sliding test. Images in Figure 12A and 12B were acquired using secondary electrons, whereas images in Figure 12C and 12D were obtained using HD-BSD imaging in a topography-sensitive configuration. In all images, the worn surfaces exhibit pronounced grooves aligned with the sliding direction, confirming that plowing is one of the dominant wear mechanisms. These grooves are associated with the action of hard asperities or entrapped wear debris acting as third bodies, which penetrate the softer aluminum surface and displace material along the sliding path. In addition to the plowing marks, the wear tracks display clear evidence of adhesive wear. The presence of delaminated areas, material pull-out, and plastically deformed regions indicates that repeated adhesion and rupture events occurred during sliding. In particular, the higher magnification Figure 12D reveals the formation of layered and cracked tribolayers, which are characteristic of mechanically mixed transfer layers formed under dry sliding conditions. The cracking and partial detachment of these layers suggest an unstable tribological contact, consistent with the large fluctuations observed in the COF.

Overall, the SEM observations confirm that the wear behavior of the WAAM-fabricated Al5356 samples is governed by a mixed wear mechanism, in which adhesive wear is predominant and accompanied by an abrasive/plowing contribution. This interpretation is in agreement with the confocal microscopy results and the measured wear coefficients.

When comparing the wear scars among the different samples, no major qualitative differences are observed. The wear tracks exhibit comparable widths and depths, indicating that the overall wear severity is similar regardless of the WAAM deposition mode employed. Although slight local variations can be detected, such as marginally deeper or more uneven profiles in certain cases, these do not translate into marked differences in the calculated wear volumes.

Therefore, although minor trends can be identified in Figure 13, such as the lower average COF for the cold arc condition, the strong overlap of the experimental data indicates that no conclusive differences in frictional or wear behavior can be established among the three WAAM processing modes. Overall, the wear track morphology corroborates the quantitative tribological results, confirming a predominantly adhesive wear regime with an accompanying plowing component for all conditions studied.

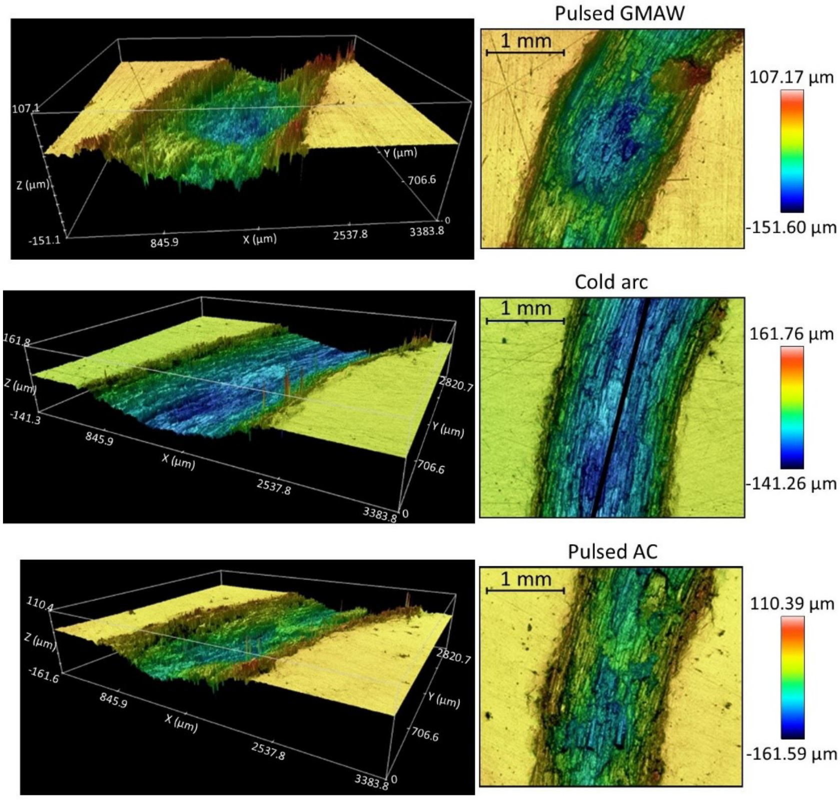

Figure 11. Representative confocal microscopy images of wear tracks for the pulsed GMAW, cold arc, and pulsed AC samples after dry sliding tests

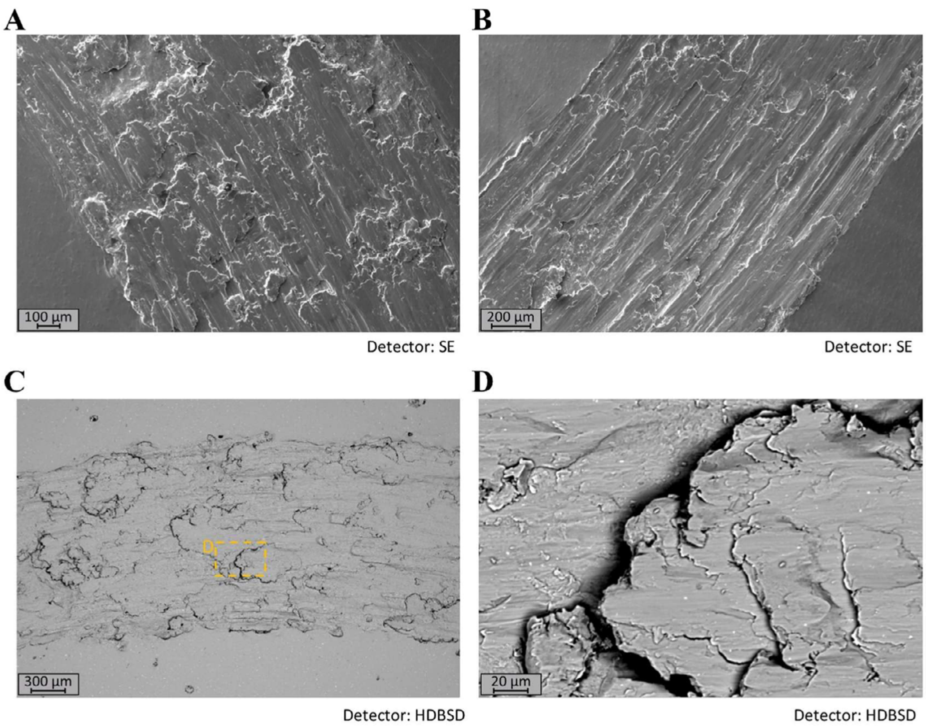

Figure 12. Scanning electron micrographs of a representative wear track: (A, B) secondary electron (SE) images and (C, D) high-definition backscattered electron (HDBSD) images with enhanced topographic contrast. Scale bars: 100 µm/200 µm/300 µm/20 µm; magnification: 150×/125×/70×/1,000×.

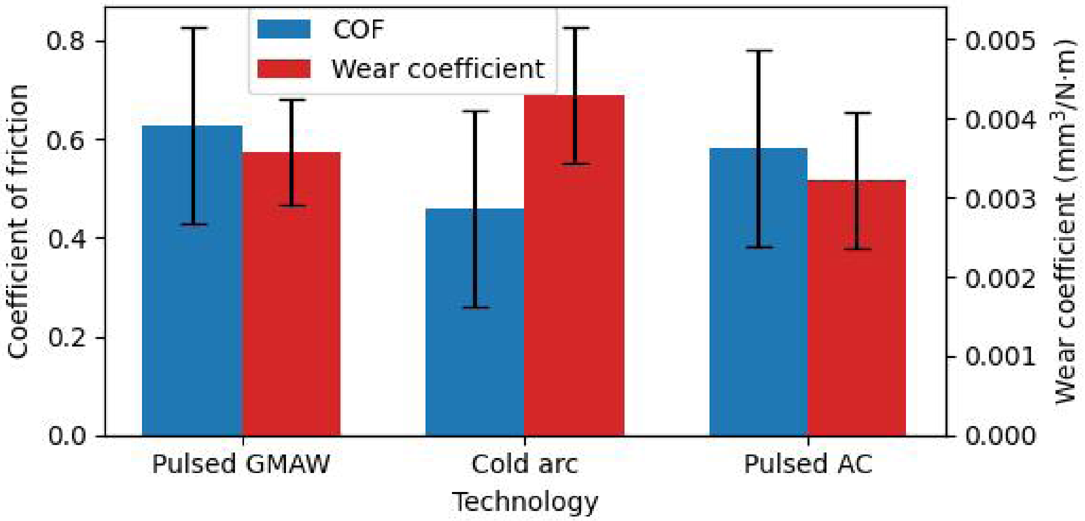

Figure 13. Mean values and standard deviations of the coefficient of friction (COF) and wear coefficient for the wire arc additive manufacturing-fabricated Al5356 samples under dry sliding conditions

4. Conclusion

This study evaluated the influence of different GMAW-based WAAM deposition modes (pulsed GMAW, cold arc, and pulsed AC) on the microstructure, hardness, wear behavior, and corrosion resistance of Al5356 walls. Based on the obtained results, the following conclusions can be drawn:

- The microstructural analysis showed that the deposition mode substantially affects grain size, Mg distribution, and porosity. Pulsed AC exhibited the largest grain size, pulsed GMAW an intermediate one, and cold arc the finest microstructure. These differences are consistent with the different heat input levels and arc characteristics of each process, which control thermal gradients, cooling rates, and thermal cycling during deposition. In addition, Mg segregation at grain boundaries was observed in all conditions, with possible formation of β (Al_3Mg_2) phase under localized thermal exposure, which contributes to microstructural heterogeneity.
- The electrochemical tests carried out in 0.6 M NaCl solution revealed moderate to low overall corrosion rates for all WAAM-fabricated samples. While the corrosion potentials of the three conditions were relatively similar, the corrosion current density showed clear differences depending on the deposition mode. The pulsed AC condition exhibited the most favorable corrosion performance, with the lowest mean Icorr among the three conditions, which may be associated with its lower porosity and coarser grain structure, resulting in a lower density of grain boundaries available for Mg segregation and possible β-phase precipitation. The corrosion behavior of all samples was also strongly influenced by intergranular attack, associated with Mg-enriched grain boundary regions and localized galvanic effects.
- The average hardness measured along the walls was comparable for all deposition modes, although slight variations were observed. Pulsed AC showed marginally lower hardness values, which can be attributed to its larger grain size and lower grain boundary density, in agreement with the Hall–Petch relationship and reduced boundary strengthening. Moreover, pulsed AC also exhibited the most homogeneous hardness distribution along the wall. In contrast, pulsed GMAW and cold arc samples showed higher spatial variability, likely associated with microstructural heterogeneities, variations in grain size, and non-uniform porosity distribution.
- Regarding tribological performance, all deposition modes exhibited similar wear behavior under dry sliding conditions, with no pronounced differences in friction coefficient or wear resistance. Although minor trends were observed (such as a slightly lower friction coefficient for the cold arc condition), the overlap in experimental scatter indicates that the wear response is not strongly affected by the deposition mode under the tested conditions. This suggests that, despite differences in microstructure and porosity, the dominant wear mechanisms remain comparable across all samples.

Overall, the results demonstrate that the WAAM deposition mode clearly influences microstructural development—particularly grain size, Mg segregation, and porosity—which in turn governs corrosion behavior and hardness distribution. In contrast, its effect on tribological performance under the studied conditions appears to be limited, indicating that wear mechanisms are less sensitive to the observed microstructural variations than corrosion-related processes.

Acknowledgments

The authors would like to express their gratitude to Pablo Pujol from UCTAI (Unidad Científico-Técnica de Apoyo a la Investigación) for his support in the SEM analysis.

Funding

This research was funded by the Spanish Ministry of Science and Innovation (MCIN/AEI/10.13039/501100011033) under the project FactorIA (grant number PLEC2024-011165), with additional support from the European Union through the 2ª convocatoria clásica de proyectos del programa POCTEFA 2021–2027 project SURFAV EFA239/06.

Conflict of interest

Fernando Veiga is an Editorial Board Member of this journal, but was not in any way involved in the editorial and peer-review process conducted for this paper, directly or indirectly. The other authors declare that they have no competing interests.

Author contributions

Conceptualization: Eneko Villabona, Fernando Veiga, Pedro Rivero
Formal analysis: Eneko Villabona, Eider Aldalur
Funding acquisition: Fernando Veiga
Investigation: Eneko Villabona, Fernando Veiga, Alfredo Suárez, Eider Aldalur
Methodology: Eneko Villabona, Fernando Veiga, Eider Aldalur
Supervision: Fernando Veiga
Writing–original draft: Eneko Villabona, Alfredo Suárez
Writing–review & editing: Fernando Veiga, Pedro Rivero

Ethics approval and consent to participate

Not applicable.

Consent for publication

Not applicable.

Availability of data

The data will be made available upon request.

References

1. Svetlizky D, Das M, Zheng B, *et al*. Directed energy deposition (DED) additive manufacturing: Physical characteristics, defects, challenges and applications. *Mater Today*. 2021;49:271-295.

   doi: 10.1016/j.mattod.2021.03.020

2. Gürol U, Kocaman E, Dilibal S, Koçak M. A comparative study on the microstructure, mechanical properties, wear and corrosion behaviors of SS 316 austenitic stainless steels manufactured by casting and WAAM technologies. *CIRP J Manuf Sci Technol*. 2023;47:215-227.

   doi: 10.1016/j.cirpj.2023.10.005

3. Geng H, Li J, Xiong J, Lin X, Zhang F. Optimization of wire feed for GTAW based additive manufacturing. *J Mater Process Technol*. 2017;243:40-47.

   doi: 10.1016/j.jmatprotec.2016.11.027

4. Villabona E, Sandua X, Veiga F, Suárez A, Aldalur E, Rivero P. Corrosion analysis of plasma arc welded and gas metal arc welded 316L stainless steel in wire arc additive manufacturing. *Int J Adv Manuf Technol*. Published online October 14, 2025.

   doi: 10.1007/s00170-025-16724-z

5. Kopf T, Glück T, Gruber D, *et al*. Process modeling and control for additive manufacturing of Ti-6Al-4V using plasma arc welding - methodology and experimental validation. *J Manuf Process*. 2024;126:12-23.

   doi: 10.1016/j.jmapro.2024.07.072

6. Iván Tabernero, Paskual A, Álvarez P, Suárez A. Study on Arc Welding Processes for High Deposition Rate Additive Manufacturing. *Procedia CIRP*. 2018;68:358-362.

   doi: 10.1016/j.procir.2017.12.095

7. Köhler M, Fiebig S, Hensel J, Dilger K. Wire and Arc Additive Manufacturing of Aluminum Components. *Metals*. 2019;9(5):608.

   doi: 10.3390/met9050608

8. Derekar KS. A review of wire arc additive manufacturing and advances in wire arc additive manufacturing of aluminium. *Mater Sci Technol*. 2018;34(8):895-916.

   doi: 10.1080/02670836.2018.1455012

9. Starke EA Jr, Staley JT. Application of modern aluminium alloys to aircraft. In: *Fundamentals of Aluminium Metallurgy*. Elsevier; 2011:747-783.

   doi: 10.1533/9780857090256.3.747

10. Veiga F, Villabona E, Suárez A, Rivero P, Aldalur E. LFAM with Metallic Materials—Applications. In: *Large Format Additive Manufacturing*. Published online December 5, 2025:393-438.

doi: 10.1002/9783527844807.ch14

11. Su C, Chen X, Gao C, Wang Y. Effect of heat input on microstructure and mechanical properties of Al-Mg alloys fabricated by WAAM. *Appl Surf Sci*. 2019;486:431-440.

doi: 10.1016/j.apsusc.2019.04.255

12. Tawfik MM, Nemat-Alla MM, Dewidar MM. Effect of Travel Speed on the Properties of Al-Mg Aluminum Alloy Fabricated by Wire Arc Additive Manufacturing. *J Mater Eng Perform*. 2021;30(10):7762-7769.

doi: 10.1007/s11665-021-05959-y

13. Aldalur E, Suárez A, Veiga F. Metal transfer modes for Wire Arc Additive Manufacturing Al-Mg alloys: Influence of heat input in microstructure and porosity. *J Mater Process Technol*. 2021;297:117271.

doi: 10.1016/j.jmatprotec.2021.117271

14. Aldalur E, Suárez A, Veiga F, Holgado I, Ortega N. Tomography analysis of Al–Mg alloys manufactured by wire-arc directed energy deposition with different metal transfer modes. *Alex Eng J*. 2023;82:168-177.

doi: 10.1016/j.aej.2023.10.002

15. Pépe N, Egerland S, Colegrove PA, Yapp D, Leonhartsberger A, Scotti A. Measuring the process efficiency of controlled gas metal arc welding processes. *Sci Technol Weld Join*. 2011;16(5):412-417.

doi: 10.1179/1362171810Y.0000000029

16. ASTM International. ASTM G99-17: Standard Test Method for Wear Testing with a Pin-on-Disk Apparatus. West Conshohocken, PA: ASTM International; 2021.

17. Zhao D, Long D, Niu T, Zhang T, Hu X, Liu Y. Effect of Mg Loss and Microstructure on Anisotropy of 5356 Wire Arc Additive Manufacturing. *J Mater Eng Perform*. 2022;31(10):8473-8482.

doi: 10.1007/s11665-022-06802-8

18. Liang J, Zheng Z, Xu Z, Wang S, Han H. 电弧增材5356铝合金微观组织结构及耐腐蚀行为 [Microstructure and corrosion resistance properties of 5356 aluminum alloy fabricated by wire and arc additive manufacturing]. *Cailiao Gongcheng (Mater Eng)*. 2025;53(2):115-124. [In Chinese].

doi: 10.11868/j.issn.1001-4381.2023.000648

19. Zhang J, Zhuo X, Shi M, *et al*. Near Immersion active cooling assisted WAAM of 5356 aluminum Alloy: Formability and microstructural evolution. *J Mater Res Technol*. 2025;38:5657-5667.

doi: 10.1016/j.jmrt.2025.09.036

20. Jeon MS, Huang Y, Kam DH, Oh MS, Lee KA. Interlayer integrity and mechanical anisotropy of WAAM-processed Al-Mg alloys. *J Alloys Compd*. 2025;1042:184124.

doi: 10.1016/j.jallcom.2025.184124

21. Zhang H, Yu S, Yang Z, Zhang C. The influence of porosity and precipitates on the corrosion behavior of A356 aluminum alloy. *J Electroanal Chem*. 2023;948:117796.

doi: 10.1016/j.jelechem.2023.117796

22. Lashgari HR, Xue Y, Onggowarsito C, Kong C, Li S. Microstructure, Tribological Properties and Corrosion Behaviour of Additively Manufactured 17-4PH Stainless Steel: Effects of Scanning Pattern, Build Orientation, and Single vs. Double scan. *Mater Today Commun*. 2020;25:101535.

doi: 10.1016/j.mtcomm.2020.101535

23. Sun Y, Moroz A, Alrbaey K. Sliding Wear Characteristics and Corrosion Behaviour of Selective Laser Melted 316L Stainless Steel. *J Mater Eng Perform*. 2014;23(2):518-526.

doi: 10.1007/s11665-013-0784-8

24. Su Y, Wang C, Xu X, Luo K, Lu J. Pore defects and corrosion behavior of AISI 316L stainless steel fabricated by laser directed energy deposition under closed-loop control. *Surf Coat Technol*. 2023;463:129527.

doi: 10.1016/j.surfcoat.2023.129527

25. Wang C, Jiang Z, Ma X, Zhang Y, He P, Han F. Effect of solid solution time on microstructure and corrosion property of wire arc additively manufactured 2319 aluminum alloy. *J Mater Res Technol*. 2023;26:2749-2758.

doi: 10.1016/j.jmrt.2023.08.098

26. Muthukumaran A, Jeyakumar S, Jayakumar K. Metallurgical and mechanical properties of marine grade AA5356 using wire arc additive manufacturing. *Mater Res Express*. 2024;11(7):076503.

doi: 10.1088/2053-1591/ad5817

27. Imširović M, Trdan U, Klobčar D, Bračun D, Nagode A, Berthe L. Mitigating defects in directed energy deposited aluminium 5356 alloy through in-situ workpiece vibration. *J Mater Res Technol*. 2024;33:1581-1599.

doi: 10.1016/j.jmrt.2024.09.179

28. Zuo X, Lv Z, Wang Y, Chen X, Qi W. Microstructural Organization and Mechanical Properties of 5356 Aluminum Alloy Wire Arc Additive Manufacturing Under Low Heat Input Conditions. *Metals*. 2025;15(2):116.

doi: 10.3390/met15020116

29. Wang J, Zhu K, Zhang W, Zhu X, Lu X. Microstructural and defect evolution during WAAM resulting in mechanical property differences for AA5356 component. *J Mater Res Technol*. 2023;22:982-996.

doi: 10.1016/j.jmrt.2022.11.116

30. Sharma SK, Chandra M, Kazmi KH, Shukla AK, Rajak S. Surface Characteristics, Microstructural, and Tribological Behavior of Wire Arc Additive Manufactured Aluminum-5356 Alloy. *J Mater Eng Perform*. 2025;34(4):3047-3055.

    doi: 10.1007/s11665-024-09320-x

31. Miyajima T, Iwai Y. Effects of reinforcements on sliding wear behavior of aluminum matrix composites. *Wear*. 2003;255(1-6):606-616.

    doi: 10.1016/S0043-1648(03)00066-8

32. Farhat ZN, Ding Y, Northwood DO, Alpas AT. Effect of grain size on friction and wear of nanocrystalline aluminum. *Mater Sci Eng A*. 1996;206(2):302-313.

    doi: 10.1016/0921-5093(95)10016-4

33. Thasleem P, Kumar D, Joy ML, Kuriachen B. Effect of heat treatment and electric discharge alloying on the lubricated tribology of Al–Si alloy fabricated by selective laser melting. *Wear*. 2022;494-495:204244.

    doi: 10.1016/j.wear.2022.204244